Nonadiabatic coupling in the 3 $^3\Pi$ and 4 $^3\Pi$ states of NaK

R. D. Miles,[a] L. Morgus,[b] D. O. Kashinski, J. Huennekens,[c] and A. P. Hickman[d]
Department of Physics, Lehigh University, Bethlehem, Pennsylvania 18015

(Received 11 May 2006; accepted 9 August 2006; published online 17 October 2006)

The excited 3 $^3\Pi$ and 4 $^3\Pi$ electronic states of the NaK molecule exhibit an avoided crossing, leading to the anomalous behavior of many features of the rovibrational energy levels belonging to each state. A joint experimental and theoretical investigation of these states has been carried out. Experimental measurements of the vibrational, rotational, and hyperfine structure of numerous levels of the 3 $^3\Pi$ state were recently obtained using the Doppler-free, perturbation-facilitated optical-optical double resonance technique. Additional measurements for the 4 $^3\Pi$ state as well as bound-free emission spectra from selected 3 $^3\Pi$, 4 $^3\Pi$, and mixed 3 $^3\Pi \sim 4$ $^3\Pi$ rovibrational levels are reported here. A model is also presented for calculating the mixed rovibrational level energies of the coupled 3 $^3\Pi$-4 $^3\Pi$ system, starting from a 2×2 diabatic electronic Hamiltonian. The 3 $^3\Pi$ and 4 $^3\Pi$ potential curves and the coupling between them are simultaneously adjusted to fit the observed rovibrational levels of both states. The energy levels of the potential curves determined by the fit are in excellent agreement with experiment. The nonadiabatic coupling is sufficiently strong to cause an overall shift of 2–3 cm^{-1} for many rovibrational levels as well as somewhat larger shifts for certain pairs of 3 $^3\Pi \sim 4$ $^3\Pi$ levels that would otherwise be very close together. © *2006 American Institute of Physics*. [DOI: 10.1063/1.2348635]

I. INTRODUCTION

Several high-resolution spectroscopic studies in our laboratory have probed the fine and hyperfine structure of rovibrational levels of electronically excited triplet states of NaK.[1–5] As part of this program, Morgus *et al.*[4] recently reported several anomalous features of the 3 $^3\Pi$ state that arise from the avoided crossing of the adiabatic potential curves corresponding to that state and the 4 $^3\Pi$ state. Several rovibrational level energies of the 3 $^3\Pi$ state could not be accurately described because they were significantly perturbed by levels of the 4 $^3\Pi$ state. In the present work, we report the measurement of additional rovibrational levels for the 4 $^3\Pi$ state, and we formulate a theoretical description of the coupled 3 $^3\Pi$-4 $^3\Pi$ system that rigorously includes the nonadiabatic coupling between these electronic states.

As in our previous experimental work,[1–5] we use the technique of "perturbation-facilitated, optical-optical double resonance" (PFOODR) spectroscopy[6–29] to measure excitation spectra of various rovibrational levels of excited triplet states. This technique relies on two photon excitation from the singlet ground state to a highly excited triplet state through specific, mixed, intermediate "window" levels that display both singlet and triplet character. By using narrow band continuous wave (cw) lasers, we achieve very high resolution since the technique is inherently Doppler-free.

The analysis of the two coupled electronic states (3 $^3\Pi$ and 4 $^3\Pi$) is based on a description using a 2×2 diabatic Hamiltonian matrix. Nonadiabatic coupling between two adiabatic states can be easily evaluated if those states are written as linear combinations of diabatic states and if one assumes that the R dependence of the adiabatic electronic wave functions comes entirely from the coefficients of the linear combination.[30,31] We show in the present work that this approach leads to a very convenient formalism for calculating the rovibrational energy levels of a system described by two diabatic states.

Magnier and Millié[32] and Magnier *et al.*[33] have calculated adiabatic potential curves for many excited electronic states of NaK, and their results clearly exhibit the avoided crossing between the 3 $^3\Pi$ and 4 $^3\Pi$ curves. However, they did not determine diabatic curves, which are needed to implement our coupled state formalism, so we performed new *ab initio* calculations using the block diagonalization method[34] that we have implemented to determine diabatic potentials for other systems.[35,36] The calculated diabatic potentials provide the initial approximation for a fitting procedure based on our coupled state formalism. We report calculations in which we simultaneously vary the potential curves for the 3 $^3\Pi$ and 4 $^3\Pi$ electronic states as well as the coupling between them in order to achieve an accurate fit of all the measured ro-vibrational energy levels.

This paper is organized as follows. Section II briefly describes the experiment and the data obtained. Section III A presents the theory of nonadiabatic coupling for two electronic states, and Sec. III B describes the *ab initio* electronic structure calculations. Section IV presents and discusses our main results: new rovibrational level energies for the 4 $^3\Pi$ state, bound-free spectra from mixed 3 $^3\Pi \sim 4$ $^3\Pi$ rovibrational levels, and the details of our fitting procedure and the fit obtained. Section V contains concluding remarks.

[a]Present address: Propulsion Science and Technology, Inc., 848 Town Center Drive, Langhorne, PA 19047.
[b]Present address: Department of Physics, Drew University, 36 Madison Ave., Madison, NJ 07940.
[c]Electronic mail: jph7@lehigh.edu
[d]Electronic mail: aph2@lehigh.edu

II. EXPERIMENT

The experimental setup is the same as that used in Ref. 1 and is shown in Fig. 1 of that reference. Briefly, a mixture of sodium and potassium metal in a five-arm stainless steel heat-pipe oven is heated to a temperature in the range of $T \sim 330-395\ ^\circ\mathrm{C}$, producing a vapor of NaK molecules in addition to other atomic and molecular species. Argon buffer gas with pressure in the range of 0.5–2.2 Torr is used to keep the alkali vapor away from the windows.

We use the PFOODR technique to excite some NaK molecules from the ground state $1(X)^1\Sigma^+$ to levels of either the $3\ ^3\Pi_{\Omega=0}$ or $4\ ^3\Pi_{\Omega=0}$ state through mixed $1(b)^3\Pi_{\Omega=0}(v_b,J) \sim 2(A)^1\Sigma^+(v_A,J)$ window levels $[n\ ^3\Pi_{\Omega=0}(v_{n\Pi},J\pm1) \leftarrow 1(b)^3\Pi_{\Omega=0}(v_b,J) \sim 2(A)^1\Sigma^+(v_A,J) \leftarrow 1(X)^1\Sigma^+(v_X,J\pm1)]$. A tunable, cw, single-mode dye laser (Coherent 699-29) is used to pump molecules from a selected ground state level $1(X)^1\Sigma^+(v_X,J\pm1)$ to the intermediate window levels, which are mixtures of $1(b)^3\Pi_{\Omega=0}(v_b,J)$ and $2(A)^1\Sigma^+(v_A,J)$ that are coupled together by the spin-orbit interaction. Once the pump transition of interest is found, the pump laser frequency is fixed. A tunable, cw, single-mode Ti:Sapphire laser (Coherent 899-29) is used as the probe laser to further excite molecules from the populated window level to various levels of the upper state $n\ ^3\Pi_{\Omega=0}(v_{n\Pi},J\pm1)$. The pump and probe lasers counterpropagate through the heat-pipe oven. They are gently focused and carefully overlapped at the center of the oven.

Excitation to a particular upper state level is detected by monitoring green $n\ ^3\Pi_{\Omega=0}(v_{n\Pi},J\pm1) \rightarrow 1(a)^3\Sigma^+$ fluorescence (using a photomultiplier tube equipped with appropriate filters), emitted at 90° with respect to the laser propagation direction, as the probe laser frequency is scanned over a transition. Since the pump laser has a very narrow bandwidth, only one velocity component of the intermediate level is populated by the pump laser, and the method is inherently Doppler-free. As demonstrated in Ref. 1, the intermediate state hyperfine structure is strongly suppressed when counterpropagating laser beams are used, so that the hyperfine structure of the upper state can be resolved. Pump laser frequencies are calibrated using an iodine reference cell and comparing measured I_2 spectral lines to values listed in the iodine atlas.[37] Probe laser frequencies are calibrated using optogalvanic signals from neon transitions in a hollow cathode lamp. We believe that absolute energies of $3\ ^3\Pi$ and $4\ ^3\Pi$ rovibrational levels are accurate to $\sim 0.02\ \mathrm{cm}^{-1}$. However, hyperfine splittings are determined with a much higher precision of $\sim 0.001\ \mathrm{cm}^{-1}$.

Resolved fluorescence scans can also be recorded. In this case, both pump and probe laser frequencies are fixed, and fluorescence is sent through a 0.3 m monochromator (McPherson model 218). Monochromator slits are typically set to $\sim 200\ \mu$m, yielding a resolution of about 0.5 nm. Further details of the experimental setup can be found in previous reports.[1,4,38]

III. THEORY

We consider the problem of calculating the overlapping rovibrational energy levels of two coupled electronic potential energy surfaces such as those shown in Fig. 1. Section III A describes our method for calculating the rovibrational levels of the coupled $3\ ^3\Pi$ and $4\ ^3\Pi$ electronic states, starting from diabatic potential curves. Section III B describes the *ab initio* calculations we performed to determine plausible diabatic curves.

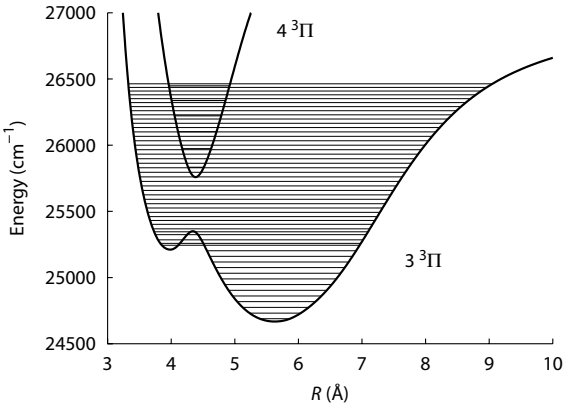

FIG. 1. The $3\ ^3\Pi$ and $4\ ^3\Pi$ potential curves of NaK and their overlapping vibrational levels.

A. Nonadiabatic coupling for two electronic states

The radial Schroedinger equation for a diatomic molecule can be written as

$$[\hat{H} - E]\Psi(R,q) = 0, \tag{1}$$

where

$$\hat{H} = -\frac{\hbar^2}{2\mu}\frac{d^2}{dR^2} + \hat{H}_{\mathrm{elec}}(R,q) + V_{\mathrm{c}}(R), \tag{2}$$

μ is the reduced nuclear mass, R is the internuclear separation, q denotes collectively all the electronic coordinates, $\hat{H}_{\mathrm{elec}}(R,q)$ is the electronic Hamiltonian, and V_{c} is the centrifugal potential,

$$V_{\mathrm{c}}(R) = \frac{[J(J+1) - \Omega^2]\hbar^2}{2\mu R^2}. \tag{3}$$

J and Ω determine the total angular momentum and its projection along the internuclear axis, respectively.

We look for a solution $\Psi(R,q)$ to Eq. (1) as a sum over vibrational-electronic functions,

$$\Psi(R,q) = \sum_{\alpha}\sum_{v} \chi^J_{\alpha v}(R)\psi^{\mathrm{ad}}_{\alpha}(R,q), \tag{4}$$

where α denotes the electronic state ($3\ ^3\Pi$ and $4\ ^3\Pi$) and each $\psi^{\mathrm{ad}}_{\alpha}(R,q)$ is an adiabatic eigenfunction of $\hat{H}_{\mathrm{elec}}$,

$$\hat{H}_{\mathrm{elec}}(R,q)\psi^{\mathrm{ad}}_{\alpha}(R,q) = E_{\alpha}(R)\psi^{\mathrm{ad}}_{\alpha}(R,q). \tag{5}$$

The $\psi^{\mathrm{ad}}_{\alpha}(R,q)$ are orthonormal with respect to integration over the electronic coordinates q.

The usual procedure leading to the Born-Oppenheimer approximation is to substitute Eq. (4) into Eq. (1) and then to neglect the derivatives of $\psi^{\mathrm{ad}}_{\alpha}(R,q)$ with respect to R. One arrives at a separate nuclear radial equation for each electronic state, whose solutions are the rovibrational eigenfunc-

tions. For the present case, however, one does not expect the R derivatives of the 3 $^3\Pi$ and 4 $^3\Pi$ electronic functions to be negligible near the avoided crossing. An alternative procedure is to express the adiabatic functions (two in the present case) in terms of diabatic functions $\psi_\alpha^{\mathrm{dia}}(q)$,

$$\psi_1^{\mathrm{ad}}(R,q) = \cos\,\theta(R)\psi_1^{\mathrm{dia}}(q) - \sin\,\theta(R)\psi_2^{\mathrm{dia}}(q), \tag{6}$$

$$\psi_2^{\mathrm{ad}}(R,q) = \sin\,\theta(R)\psi_1^{\mathrm{dia}}(q) + \cos\,\theta(R)\psi_2^{\mathrm{dia}}(q). \tag{7}$$

To emphasize that the diabatic functions usually have a much weaker dependence on R, we have dropped the R from our notation. It has been pointed out[30,31] that the expansion given by Eqs. (6) and (7) enables the R derivatives of the adiabatic wave functions to be evaluated in terms of the derivatives of $\theta(R)$.

We now look for a solution to Eq. (1) that has the form of Eq. (4), without the expectation that the coupling between the electronic states will be neglected. We will regard Eq. (4) as a double sum over vibrational-electronic basis functions labeled by the indices α and v. The exact form of the functions $\chi_{\alpha v}^J(R)$ will not be specified until later, although we assume that they form an orthonormal set. We can find the eigenfunctions of Eq. (1) by diagonalizing the matrix representation of $\hat{H}$,

$$H_{\alpha v,\alpha' v'}^J = \int\int \chi_{\alpha v}^J(R)\psi_\alpha^{\mathrm{ad}}(R,q)\hat{H}\chi_{\alpha' v'}^J(R)\psi_{\alpha'}^{\mathrm{ad}}(R,q)dRdq. \tag{8}$$

All of the terms in Eq. (8), including the effect of the d^2/dR^2 operator on the basis function $\chi_{\alpha' v'}^J(R)\psi_{\alpha'}^{\mathrm{ad}}(R,q)$, can be evaluated exactly using the expansion in Eqs. (6) and (7). Using trigonometry and integration by parts, we obtain

$$H_{\alpha v,\alpha' v'}^J = \delta_{\alpha,\alpha'}\int \chi_{\alpha v}^J(R)\left[-\frac{\hbar^2}{2\mu}\frac{d^2}{dR^2} + E_\alpha(R) + V_c(R) + \frac{\hbar^2}{2\mu}\left(\frac{d\theta}{dR}\right)^2\right]\chi_{\alpha' v'}^J(R)dR$$
$$+ (1-\delta_{\alpha,\alpha'})\frac{\hbar^2}{2\mu}\int\left[\frac{d\chi_{\alpha v}^J}{dR}\chi_{\alpha' v'}^J - \chi_{\alpha v}^J\frac{d\chi_{\alpha' v'}^J}{dR}\right]\frac{d\theta}{dR}dR \quad \text{for } \alpha \leqslant \alpha'. \tag{9}$$

The restriction $\alpha \leqslant \alpha'$ is based on the convention $\alpha=1$ for 3 $^3\Pi$ and $\alpha=2$ for 4 $^3\Pi$. One should use Eq. (9) to construct the upper triangular part of the matrix and then invoke symmetry.

The first term on the right hand side of Eq. (9) suggests a natural definition of the $\chi_{\alpha v}^J(R)$. We will require these functions to be eigenfunctions associated with the eigenvalues $E_{\alpha v}^{J(0)}$ of the following radial Schroedinger equation:

$$\left[-\frac{\hbar^2}{2\mu}\frac{d^2}{dR^2} + E_\alpha(R) + V_c(R) + \frac{\hbar^2}{2\mu}\left(\frac{d\theta}{dR}\right)^2 - E_{\alpha v}^{J(0)}\right]\chi_{\alpha v}^J(R) = 0. \tag{10}$$

In other words, the functions $\chi_{\alpha v}^J(R)$ and the eigenvalues $E_{\alpha v}^{J(0)}$ are the vibrational wave functions and energies for two potential curves that are slightly modified from the pure Born-Oppenheimer 3 $^3\Pi$ and 4 $^3\Pi$ potentials. Each effective potential is formed by adding an additional term to the adiabatic Born-Oppenheimer potential,

$$V_{\mathrm{eff}}^\alpha(R) = E_\alpha(R) + \frac{\hbar^2}{2\mu}\left(\frac{d\theta}{dR}\right)^2. \tag{11}$$

The rovibrational functions $\chi_{\alpha v}^J(R)$ and the corresponding energies $E_{\alpha v}^{J(0)}$ that solve Eq. (10) can easily be determined numerically by using, for example, Le Roy's code LEVEL.[39] The superscript zero is a reminder that the energies $E_{\alpha v}^{J(0)}$ are calculated for two potential curves before the coupling between them is included.

With the definitions of the functions $\chi_{\alpha v}^J(R)$ given above, the matrix elements of $\hat{H}$ can be written in final form as

$$H_{\alpha v,\alpha' v'}^J = \delta_{\alpha,\alpha'}\delta_{v,v'}E_{\alpha v}^{J(0)} + (1-\delta_{\alpha,\alpha'})\frac{\hbar^2}{2\mu}\int\left[\frac{d\chi_{\alpha v}^J}{dR}\chi_{\alpha' v'}^J - \chi_{\alpha v}^J\frac{d\chi_{\alpha' v'}^J}{dR}\right]\frac{d\theta}{dR}dR \quad \text{for } \alpha \leqslant \alpha'. \tag{12}$$

The matrix of $\hat{H}$ defined by Eq. (12) is in block form

$$H_{\alpha v,\alpha' v'}^J \rightarrow \left(\begin{array}{c|c} 3\,^3\Pi \text{ block} & \text{nonadiabatic} \\ \text{(diagonal)} & \text{coupling terms} \\ \hline \text{nonadiabatic} & 4\,^3\Pi \text{ block} \\ \text{coupling terms} & \text{(diagonal)} \end{array}\right). \tag{13}$$

The diagonal elements are the "unperturbed" rovibrational energies $E_{\alpha v}^{J(0)}$ for the modified 3 $^3\Pi$ and 4 $^3\Pi$ potentials given by Eq. (11). The energies of the coupled system are found by diagonalizing the matrix. The eigenvectors of the matrix give the mixing coefficients of each state.

TABLE I. The long range orbitals used to augment the TZV basis set for the present calculations.

Na orbital	Exponent	K orbital	Exponent
s	0.007 66	*s*	0.006 00
d	0.271 90	*p*	0.063 90
d	0.090 64	*p*	0.019 80
d	0.028 90	*p*	0.005 20
d	0.010 00	*d*	0.173 20
		d	0.057 74
		d	0.026 60
		d	0.005 00

TABLE II. Orbital occupancies for the six CSF's that contribute significantly to the first five $^3\Pi$ adiabatic states. The bonding and antibonding orbitals σ and σ^* are related to the $3s_{\mathrm{Na}}$ and $4s_{\mathrm{K}}$ atomic orbitals by Eq. (14).

CSF	Orbital occupancy (excluding core)
Φ_1	$(\sigma)^1(\pi_{\mathrm{K}(4p)})^1$
Φ_2	$(\sigma^*)^1(\pi_{\mathrm{Na}(3p)})^1$
Φ_3	$(\sigma)^1(\pi_{\mathrm{K}(3d)})^1$
Φ_4	$(\sigma)^1(\pi_{\mathrm{K}(5p)})^1$
Φ_5	$(\sigma)^1(\pi_{\mathrm{K}(4d)})^1$
Φ_6	$(\sigma)^1(\pi_{\mathrm{Na}(3p)})^1$

B. *Ab initio* calculation of diabatic potentials

We have used the block diagonalization method[34] to calculate the diabatic potentials. This method provides an effective technique for transforming the results of a standard electronic structure calculation, which we performed using the GAMESS code,[40] into diabatic potential curves. One obtains diabatic potentials of comparable accuracy to the adiabatic potentials.

Our calculations for NaK are similar to the ones we have performed for other systems.[35,36] The general procedure involves multiconfiguration self-consistent field (MCSCF) calculations at each value of R, then a rotation of the molecular orbitals in the active space to bring them to a form close to so-called "reference" orbitals, which are defined in a way that minimizes their variation with R. Finally, a configuration interaction (CI) calculation is performed to determine the adiabatic and diabatic energies.

For this discussion, we will focus on the features specific to NaK, such as the basis set and the definition of the reference orbitals. The basis set was Dunning's triple-zeta valence basis set (TZV),[41] augmented by long range orbitals used to describe excited states. The basis set was designed to represent accurately the first several excited electronic states of NaK. Asymptotically, these states included the $3S$ and $3P$ of Na and the $4S$, $4P$, $5S$, $3D$, and $5P$ of K. The added orbitals are listed in Table I.

For the MCSCF calculations of states of $^3\Pi$ symmetry, we used an active space of two σ and five π orbitals for the two valence electrons. The two σ orbitals correlate with the asymptotic $3s_{\mathrm{Na}}$ and $4s_{\mathrm{K}}$ orbitals, and the five π orbitals correlate with the asymptotic $3p_{\mathrm{Na}}$, $4p_{\mathrm{K}}$, $5p_{\mathrm{K}}$, $3d_{\mathrm{K}}$, and $4d_{\mathrm{K}}$ orbitals. We minimized the sum of the energies of the five lowest $^3\Pi$ states. After the MCSCF calculations, we rotated the converged σ orbitals to match the ground state and first excited state σ orbitals of NaK^+, which were obtained by separate unrestricted Hartree-Fock (UHF) calculations at the same value of R. The two σ orbitals thereby obtained have a very clear interpretation. At large R, one becomes $3s_{\mathrm{Na}}$, and the other becomes $4s_{\mathrm{K}}$. As R decreases, there is a gradual transformation to a pair of orbitals that can be characterized as a bonding/antibonding pair,

$$\sigma \approx \frac{1}{\sqrt{2}}(3s_{\mathrm{Na}} + 4s_{\mathrm{K}}), \quad \sigma^* \approx \frac{1}{\sqrt{2}}(3s_{\mathrm{Na}} - 4s_{\mathrm{K}}). \tag{14}$$

We rotate the five π orbitals to match reference orbitals that were obtained as follows. We initially performed MCSCF calculations at a very large value of R ($10\,000a_0$) that determined the excited atomic orbitals $4p_{\mathrm{K}}$, $3p_{\mathrm{Na}}$, $3d_{\mathrm{K}}$, $5p_{\mathrm{K}}$, and $4d_{\mathrm{K}}$. At each smaller R, for the π orbitals, we defined a set of "shifted orbitals" using the same expansion coefficients in terms of the atomic orbitals. These orbitals were normalized and then symmetrically orthogonalized[42] to obtain the π reference orbitals. This procedure has been shown[43] to produce the set of orthonormal orbitals closest to the original set.

The next step was to perform a CI calculation using the converged and rotated orbitals. We froze the NaK^{++} core and did a full CI calculation for the two valence electrons. The number of configuration state functions (CSF's) for this calculation was 1525. The dimension of the diabatic Hamiltonian that we initially calculated was determined by investigating which CSF's contributed most strongly to the 3 $^3\Pi$ and 4 $^3\Pi$ adiabatic eigenfunctions. We found that six CSF's contribute significantly to the first five electronic states. These six CSF's are shown in Table II. Therefore, we set the dimension of the diabatic matrix to six.

The diagonal elements of $\mathbf{H}_{\mathrm{dia}}$ are shown in Fig. 2. The potentials determined by our UHF calculation for the ground state and the first excited state of NaK^+ are also shown. The curves have not been shifted to the experimental asymptotic values. There are three types of curves. Curves in the first class are roughly parallel to the ground state NaK^+ curve, which asymptotically approaches $Na(3s)+K^+$. The occupied orbitals for these curves include the bonding σ orbital described by Eq. (14). Curves in the second class are roughly parallel to the excited state NaK^+ curve, which asymptotically approaches $Na^+ + K(4s)$. The occupied orbitals for these curves include the antibonding σ^* orbital described by Eq. (14). The final class corresponds to ion pair states that separate to $Na^- + K^+$. The dashed curves in Fig. 2 are the adiabatic 2 $^3\Pi$, 3 $^3\Pi$, and 4 $^3\Pi$ potential curves. Close examination of these curves indicates that the 3 $^3\Pi$ adiabatic potential results from several diabatic potentials. The inner well is formed from the σ-type curve with the asymptote $Na(3s)+K(5p)$. The barrier is a result of the crossing between this curve and the repulsive σ^* curve that dissociates to $Na(3p)+K(4s)$. We note that the ion pair curve cuts through and mixes with the repulsive σ^* curve and the $Na(3s)+K(3d)$ σ curve in the range from $R=10$ a_0 to 16 a_0 to form the outer well. Finally, the 4 $^3\Pi$ potential is composed of the $Na(3s)+K(5p)$ σ curve and the σ^* $Na(3p)+K(4s)$ curve.

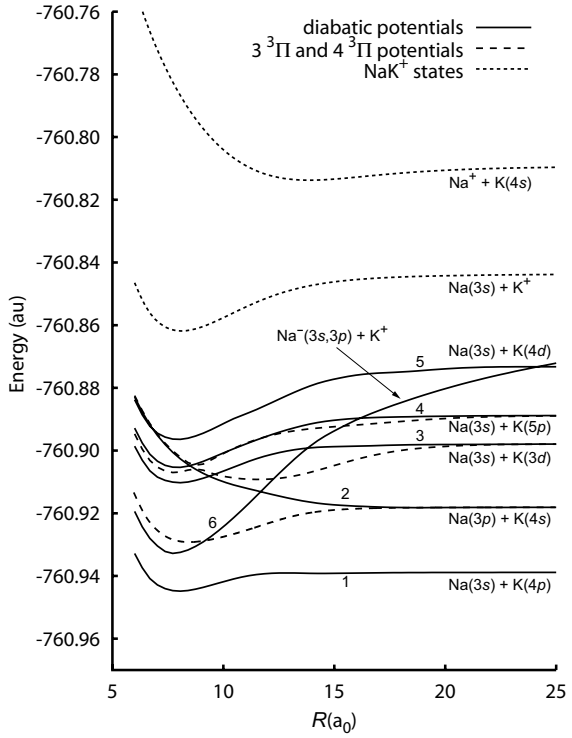

FIG. 2. *Ab initio* $^3\Pi$ diabatic potentials for NaK and adiabatic potentials for NaK^+. The $^3\Pi$ diabatic potentials are numbered 1–6 in ascending order, according to the energy of their asymptotes. The 2 $^3\Pi$, 3 $^3\Pi$, and 4 $^3\Pi$ adiabatic potentials are shown with dashed lines. At different regions of R, the 3 $^3\Pi$ potential has significant contributions from four different diabatic potentials.

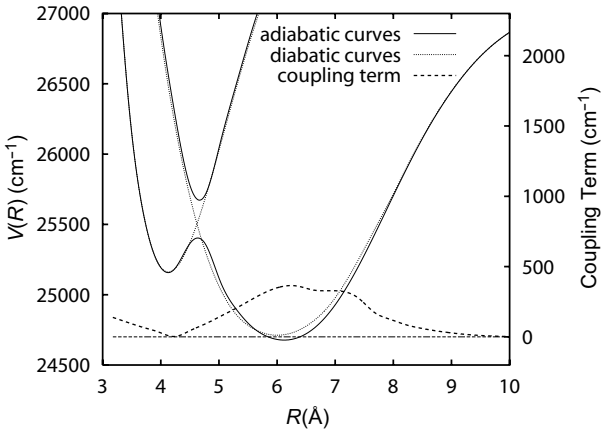

FIG. 3. *Ab initio* 2×2 adiabatic and diabatic representations for the 3 $^3\Pi$ and 4 $^3\Pi$ states. The coupling term is the off diagonal element of the diabatic matrix. The positions of the calculated minimum energies for the inner and outer wells of the 3 $^3\Pi$ adiabatic potential are 4.13 and 6.12 Å, respectively. The difference in the energies calculated for the inner and outer minima of that potential is 480.0 cm^{-1}. (Compare Fig. 8, which gives the corresponding fitted values.)

For the present application, we reduce the 6×6 diabatic representation to a simpler, 2×2 form that only includes the 3 $^3\Pi$ and 4 $^3\Pi$ states. This 2×2 representation accurately describes the diabatic crossing that forms the avoided crossing between the adiabatic 3 $^3\Pi$ and 4 $^3\Pi$ states, but it models the coupled diabatic states at the bottom of the outer well of the 3 $^3\Pi$ adiabatic potential by a single effective potential. The nonadiabatic coupling of the 2 $^3\Pi$ and 3 $^3\Pi$ states is much weaker than the coupling of the 3 $^3\Pi$ and 4 $^3\Pi$ states. As one can see from the adiabatic (dashed) curves in Fig. 2, the change in the electronic wave function at the bottom of the outer well of the 3 $^3\Pi$ adiabatic potential is much more gradual than it is near the 3 $^3\Pi$-4 $^3\Pi$ avoided crossing. The rovibrational levels localized in this part of the 3 $^3\Pi$ adiabatic potential could be well fitted by a single potential, so simplifying the coupling there appears justified.

To obtain the desired 2×2 diabatic representation, we must rearrange the 6×6 $\mathbf{H}_{\mathrm{dia}}$ into blocks. We isolate the σ curve that correlates with the asymptotic limit Na(3s) +K(5p). This curve is the one that dominates the inner well of the adiabatic 3 $^3\Pi$ state. We rearrange $\mathbf{H}_{\mathrm{dia}}$ so that this element is in the (1, 1) position. We denote the rearranged matrix $\mathbf{H}'_{\mathrm{dia}}$. Then we evaluate $\mathbf{T}^{\dagger}\mathbf{H}'_{\mathrm{dia}}\mathbf{T}$, where $\mathbf{T}$ has the following block form:

$$\mathbf{T} = \left(\begin{array}{c|c} 1 & 0 \\ \hline 0 & \mathbf{T}(5\times 5) \end{array}\right), \tag{15}$$

and $\mathbf{T}(5\times5)$ is the transformation that diagonalizes the lower 5×5 block of $\mathbf{H}'_{\mathrm{dia}}$. When we apply $\mathbf{T}$ to $\mathbf{H}'_{\mathrm{dia}}$, we obtain a new matrix whose lower 5×5 block is diagonal but has nonzero elements in the first row and column. We can identify one of the lower diagonal elements as a composite state corresponding to the outer well of the 3 $^3\Pi$ adiabatic potential. This element, the (1, 1), and the elements from the first row and column that couple them form the desired 2×2 diabatic potential. The diagonal and off diagonal elements of this matrix are shown in Fig. 3.

IV. RESULTS AND DISCUSSION

A. Experimental results

1. Level energies for the 3$^3\Pi$ and 4 $^3\Pi$ electronic states

Measured energies for 40 levels of the $^{23}Na^{39}K$ 4 $^3\Pi_{\Omega=0}$ state with $0 \leqslant v \leqslant 8$ and 9 levels of the $^{23}Na^{39}K$ 4 $^3\Pi_{\Omega=2}$ state are listed in Table 1 of the Electronic Physics Auxiliary Publication Service (EPAPS) deposit associated with the present article.[44] Measured energies for 290 rovibrational levels of the $^{23}Na^{39}K$ 3 $^3\Pi_{\Omega=0}$ state with $6 \leqslant v \leqslant 53$ were previously reported[45] in EPAPS Table 2 of Ref. 4. In addition, energies for 32 levels of the $^{23}Na^{39}K$ 3 $^3\Pi_{\Omega=2}$ state and for four levels of the $^{23}Na^{41}K$ 3 $^3\Pi_{\Omega=0}$ state were also reported in that work. The vibrational levels of the minor isotopomer were useful in making the absolute vibrational numbering assignment.

Because the vibrational spacings of the 4 $^3\Pi$ state are much larger than those of the 3 $^3\Pi$ state and because levels of the 3 $^3\Pi$ state with $v < 32$ lie well below any levels of the 4 $^3\Pi$ state with the same J, most of the observed levels of the 3 $^3\Pi$ state reported in Ref. 4 are not strongly perturbed by 3 $^3\Pi \sim 4$ $^3\Pi$ nonadiabatic coupling effects. As a result, we were able to fit Dunham coefficients to the experimentally measured energies of the 3 $^3\Pi$ outer well levels and to use the inverted perturbation approximation (IPA) method[46] to obtain a mapping of an effective 3 $^3\Pi$ state potential that was able to reproduce observed energies of 264 relatively unperturbed 3 $^3\Pi_{\Omega=0}$ levels with a standard deviation of 0.24 cm^{-1}.[4] Twenty-six of the original 290 3 $^3\Pi_{\Omega=0}$ levels

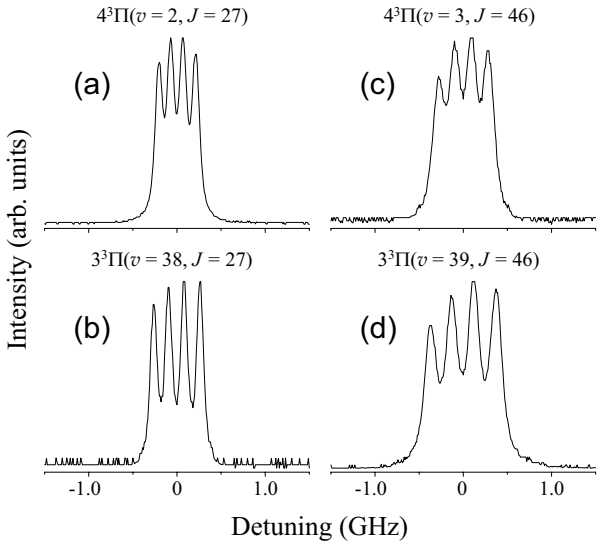

FIG. 4. Excitation spectra showing the hyperfine structure of various $3\,^3\Pi$ and $4\,^3\Pi$ rovibrational levels. The upper states for each transition are labeled in the figure, and in each case, the lower state is the predominantly triplet component of a window level $1(b)^3\Pi_{\Omega=0}(v_b, J-1) \sim 2(A)\,^1\Sigma^+(v_A, J-1)$. For scans (a) and (b) $v_b=17$ and $v_A=18$; for (c) and (d) $v_b=18$ and $v_A=20$. The measured hyperfine splittings increase with J for both electronic states. However, for levels of the same J in the same energy range, the $4\,^3\Pi$ hyperfine splittings are smaller than those of the $3\,^3\Pi$ state.

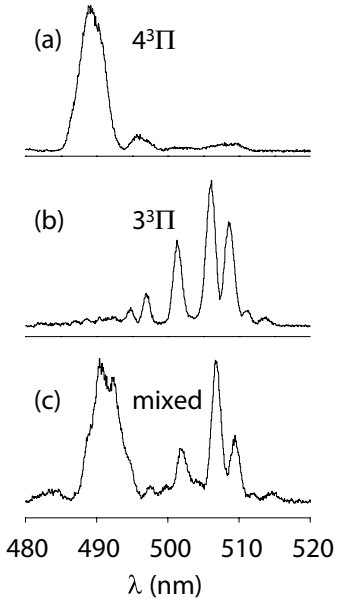

FIG. 5. Comparison of the bound-free spectra for various upper state rovibrational levels: (a) a predominantly $4\,^3\Pi$ level $[4\,^3\Pi_{\Omega=0}(v=5, J=27)]$, (b) a predominantly $3\,^3\Pi$ level $[3\,^3\Pi_{\Omega=0}(v=35, J=46)]$, and (c) a mixed level $[4\,^3\Pi_{\Omega=0}(v=1, J=27) \sim 3\,^3\Pi_{\Omega=0}(v=37, J=27)]$.

(all with $v \geqslant 32$) are more strongly affected by nonadiabatic coupling effects and were therefore excluded from the IPA fit.

On the other hand, levels of the $3\,^3\Pi$ state lying above the $4\,^3\Pi$ state minimum have vibrational spacings of $\sim 32\ \mathrm{cm}^{-1}$. Consequently, no $4\,^3\Pi$ level lies more than $16\ \mathrm{cm}^{-1}$ from a $3\,^3\Pi$ level of the same J and Ω, and as a result, all $4\,^3\Pi$ levels are strongly perturbed by nonadiabatic coupling effects. Attempts to fit Dunham coefficients to the measured $4\,^3\Pi$ energies and to carry out an IPA analysis of the $4\,^3\Pi$ state were not successful. Thus an analysis like the one presented in Sec. III A that explicitly takes into account nonadiabatic coupling effects is necessary in order to reproduce measured $4\,^3\Pi$ energies accurately. Sections IV B and IV C present the details of our determination of the 2×2 diabatic potentials that describe the $3\,^3\Pi$ and $4\,^3\Pi$ states and the resulting effects that can be ascribed to nonadiabatic coupling.

2. Bound-free spectra

Levels associated primarily with the $3\,^3\Pi$ or $4\,^3\Pi$ state are not easily distinguished from each other using just a comparison of PFOODR excitation spectra. High lying levels of the $3\,^3\Pi$ state and low lying levels of the $4\,^3\Pi$ state coexist in the same energy region, and from a particular intermediate state window level $1(b)\,^3\Pi_{\Omega=0}(v_b, J) \sim 2(A)\,^1\Sigma^+(v_A, J)$ we observe two rotational transitions (P_{11} and R_{11}) into each vibrational level of both upper states. Moreover, each transition displays a hyperfine structure pattern consisting of four peaks, with the hyperfine splittings of transitions to $4\,^3\Pi_{\Omega=0}$ levels being only slightly smaller than those associated with $3\,^3\Pi_{\Omega=0}$ levels. Figure 4 presents spectra that have been assigned to each state and illustrates how similar they can be.

Fortunately, transitions to the $3\,^3\Pi$ and $4\,^3\Pi$ states can be differentiated by considering resolved bound-free spectra. These resolved spectra correspond to fluorescence from a particular upper state rovibrational level to the continuum of levels of the $1(a)\,^3\Sigma^+$ state for fixed pump and probe laser frequencies. Figure 5 shows spectra recorded for the rovibrational levels (a) $4\,^3\Pi_{\Omega=0}(v=5, J=27)$, (b) $3\,^3\Pi_{\Omega=0}(v=35, J=46)$, and (c) for the mixed level $4\,^3\Pi_{\Omega=0}(v=1, J=27) \sim 3\,^3\Pi_{\Omega=0}(v=37, J=27)$. In Fig. 5(a), the upper level has predominantly $4\,^3\Pi$ character and the bound-free spectrum exhibits a single peak around 490 nm. In Fig. 5(b), the upper level has predominantly $3\,^3\Pi$ character and the spectrum is broader, with the major peaks in the range 502–512 nm. Figure 5(c) illustrates the interesting case where levels are strongly mixed, and the bound-free spectrum exhibits features associated with both the $3\,^3\Pi$ and $4\,^3\Pi$ states. The ratio of the emissions in the spectral regions near 490 and 508 nm is determined by the mixing amplitudes of the $3\,^3\Pi$ and $4\,^3\Pi$ rovibrational levels. In fact, by invoking a two-state model, or in some cases a three-state model, we can estimate the mixing probabilities directly from these experimental spectra (see Appendix). Table III shows, for selected levels, the comparison between the experimental mixing probablities and those calculated by the nonadiabatic coupling model. The agreement is quite good.

The differences between $3\,^3\Pi$ and $4\,^3\Pi$ bound-free spectra can be explained by considering Fig. 6, which shows the calculated NaK $3\,^3\Pi$, $4\,^3\Pi$, and $1(a)\,^3\Sigma^+$ potential curves of Magnier *et al.*[33] and the corresponding difference potentials. The analysis predicts the energy range of the bound-free spectrum for each upper state level. For the $4\,^3\Pi$ state, the vibrational functions of the narrow, V-shaped potential span

TABLE III. Experimental and calculated NaK $4\,^3\Pi(v,J) \sim 3\,^3\Pi(v',J)$ mixing amplitudes. The experimental data for each set of two or three states were analyzed separately using the model discussed in the Appendix. Except as noted, the experiments and the calculations give the same assignment of predominant $3\,^3\Pi$ or $4\,^3\Pi$ character.

			Experimental			Theoretical	
3 or $4\,^3\Pi$ assignment	v or v'	J	Energy (cm^{-1})	$3\,^3\Pi$ fraction	$4\,^3\Pi$ fraction	$3\,^3\Pi$ fraction	$4\,^3\Pi$ fraction
3	36	16	25 973.24	0.888	0.112	0.963	0.037
4	1	16	25 997.21	0.226	0.774	0.111	0.889
3	37	16	26 007.58	0.887	0.113	0.975	0.025
4[a]	1	27	26 025.10	0.430	0.570	0.580	0.421
3[a]	37	27	26 028.53	0.570	0.430	0.505	0.495
3	37	46	26 081.68	0.818	0.182	0.926	0.074
4	1	46	26 109.54	0.428	0.572	0.401	0.599
3	38	46	26 119.25	0.754	0.246	0.704	0.296
4	2	25	26 143.96	0.394	0.606	0.364	0.636
3	41	25	26 159.62	0.606	0.394	0.737	0.263
3	44	27	26 250.86	0.834	0.166	0.879	0.121
4	3	27	26 275.08	0.452	0.548	0.462	0.538
3	45	27	26 289.84	0.714	0.286	0.707	0.293
3	48	14	26 354.53	0.721	0.279	0.886	0.114
4	4	14	26 360.41	0.279	0.721	0.216	0.784
3	49	44	26 442.41	0.823	0.177	0.897	0.103
4	4	44	26 465.28	0.400	0.600	0.422	0.578
3	50	44	26 474.99	0.777	0.223	0.745	0.255
4	5	27	26 498.39	0.231	0.769	0.180	0.820
3	53	27	26 512.60	0.769	0.231	0.914	0.086

[a]Assignment of predominant character ($3\,^3\Pi$ or $4\,^3\Pi$) based on the experimental mixing amplitudes.

a small range of R, leading to predicted emission over the relatively narrow range 479–490 nm. The single peak shown in Fig. 5(a) is consistent with this prediction, although one might expect to see more oscillations in the spectrum since the upper state vibrational level is $v=5$. However, the $4\,^3\Pi$–$1(a)\,^3\Sigma^+$ transition dipole moment $\mu(R)$ exhibits a sharp dependence on R near the avoided crossing of the $4\,^3\Pi$ and $3\,^3\Pi$ curves, switching from high values to low values with increasing R. [The $3\,^3\Pi$–$1(a)\,^3\Sigma^+$ transition dipole moment exhibits a complementary change.] The strong R dependence of $\mu(R)$ cuts off additional oscillations in the $4\,^3\Pi \rightarrow 1(a)\,^3\Sigma^+$ bound-free spectra that would otherwise be observable at shorter wavelengths. The vibrational functions of the $3\,^3\Pi$ potential exhibit more nodes and extend over a larger range of R. As a result the predicted spectrum is broader and extends over the range 475–543 nm. Experimentally, we observe $4\,^3\Pi \rightarrow 1(a)\,^3\Sigma^+$ emission between 485 and 495 nm and $3\,^3\Pi \rightarrow 1(a)\,^3\Sigma^+$ emission primarily in the range 502–512 nm.

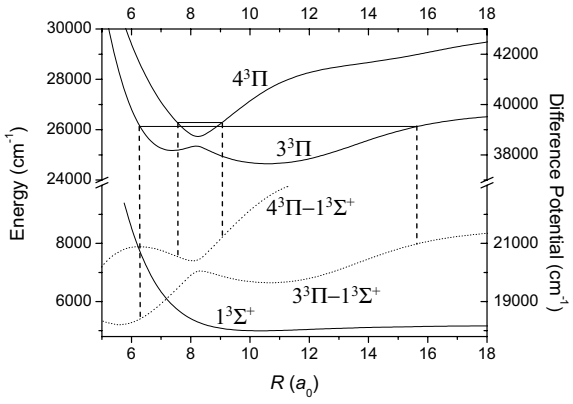

FIG. 6. Illustration of the relation between the difference potentials for the upper and lower electronic states of a bound-free transition and the expected energy (wavelength) range of the observed spectrum. The minimum and maximum values of the difference potentials between the dashed lines for each initial state provide an estimate of the energy range for the bound-free spectra, as discussed in the text.

B. Adjustment of *ab initio* diabatic potentials to fit the data

In Sec. III A, we analyzed the coupling between the $3\,^3\Pi$ and $4\,^3\Pi$ electronic states and we discussed the need to treat these two states together. We describe this coupled system by specifying the 2×2 electronic Hamiltonian matrix in the diabatic representation

$$\mathbf{H}_{\mathrm{dia}}(R)=\begin{pmatrix} V_{11}(R) & V_{12}(R) \\ V_{12}(R) & V_{22}(R) \end{pmatrix}. \tag{16}$$

In order to determine the best diabatic Hamiltonian for the coupled states, we have developed flexible analytic forms for the functions $V_{11}(R)$, $V_{12}(R)$, and $V_{22}(R)$. These analytic functions depend on parameters that can be adjusted to achieve agreement with experimental data.

We obtain the adiabatic potential curves and the mixing angle θ by direct diagonalization of Eq. (16), and then we apply the formalism of Sec. III A to calculate the rovibrational energy levels, including the effects of nonadiabatic coupling. By iteratively varying the parameters of the analytic curves, we match the calculated rovibrational energy levels of the $3\,^3\Pi$ and $4\,^3\Pi$ states to the experimental energy levels. We determine initial estimates for the fitting parameters from our *ab initio* calculations.

1. Analytic form for the potentials

We express each diagonal diabatic potential [denoted generically here by $V(R)$] using a function that has different analytic forms depending on whether R is less than or greater than R_e, the point where $V(R)$ has its minimum,

$$V(R)=\begin{cases} V_1(R) & \text{if } R \leqslant R_e \\ V_2(R) & \text{if } R > R_e. \end{cases} \tag{17}$$

We use a generalization of the Morse potential for $R \leqslant R_e$,

$$V_1(R)=Dx(x-2)+V_\infty, \tag{18}$$

where

$$x=\exp\left[-\sum_{n=1}^{N_\beta}\beta_n(R-R_e)^n\right]. \tag{19}$$

For $R>R_e$,

$$V_2(R)=\frac{\sum_{n=0}^{N_A}A_n(R-R_e)^n}{(R/R_e)^{N_A+6}}+V_\infty. \tag{20}$$

When R approaches R_e, Eq. (20) simplifies to a power series, and as $R\to\infty$ it becomes an inverse power series whose leading term behaves as $1/R^6$, as it should.

We require that the functions $V_1(R)$ and $V_2(R)$ join smoothly at R_e. Requiring continuity of $V(R)$ and its first two derivatives at R_e leads to a set of three algebraic equations that can be solved to determine A_0, A_1, and A_2. The results are

$$A_0=-D, \tag{21}$$

$$A_1=-D\frac{N_A+6}{R_e}, \tag{22}$$

$$A_2=D\left(\beta_1^2-\frac{(N_A+5)(N_A+6)}{2R_e^2}\right). \tag{23}$$

We used separate sets of parameters to define the two diagonal diabatic potentials. The off diagonal, diabatic coupling function was defined by

TABLE IV. The parameters of the best fit for the diagonal elements of the diabatic Hamiltonian for the coupled $3\,^3\Pi$-$4\,^3\Pi$ system. The parameters are defined in Eqs. (17)–(23); those marked with an asterisk (*) were not varied in the fit.

Parameter	Inner well value	Outer well value
V_∞^*	$2.998\,400\times10^4$ cm^{-1}	$2.680\,913\,2\times10^4$ cm^{-1}
R_e	3.983 46 Å	5.712 30 Å
D	$4.765\,11\times10^3$ cm^{-1}	$2.116\,31\times10^3$ cm^{-1}
N_β^*	5	5
β_1	-5.6047×10^{-1} Å^{-1}	$4.309\,36\times10^{-1}$ Å^{-1}
β_2	5.725×10^{-1} Å^{-2}	3.3389×10^{-2} Å^{-2}
β_3	-4.718×10^{-1} Å^{-3}	-2.3364×10^{-2} Å^{-3}
β_4	-2.177 Å^{-4}	-1.1616×10^{-2} Å^{-4}
β_5	-3.184 Å^{-5}	9.063×10^{-4} Å^{-5}
N_A^*	9	8
A_3	-1.6650×10^4 Å^{-3}	-2.1502×10^3 Å^{-3}
A_4	-4.1139×10^4 Å^{-4}	$-3.203\,07\times10^3$ Å^{-4}
A_5	1.0311×10^4 Å^{-5}	$1.915\,47\times10^3$ Å^{-5}
A_6	3.054×10^3 Å^{-6}	-4.6587×10^2 Å^{-6}
A_7	-9.95×10^2 Å^{-7}	3.9661×10^1 Å^{-7}
A_8	-4.381×10^3 Å^{-8}	6.57×10^{-1} Å^{-8}
A_9	7.47×10^2 Å^{-9}	

$$H_{12}(R)=[A+B(R-R_0)]e^{-\gamma(R-R_0)^2}. \tag{24}$$

This off diagonal term is most important near the crossing point of the diabatic potentials. The value of R_0 in Eq. (24) was chosen to give the maximum flexibility of the function near the crossing point and to ensure that the function behaves in a benign way far from the crossing point.

2. Nonlinear fitting methodology and results

The parameters of the functions defined above were adjusted in order to achieve the best possible agreement between the measured and calculated rovibrational energy levels for the $3\,^3\Pi$ and $4\,^3\Pi$ states. We used a general implementation of the Levenberg-Marquardt algorithm[47] and wrote specific subroutines that evaluated elements of the diabatic Hamiltonian. We also used a slightly modified version of LEVEL 7.5 (Ref. 39) to calculate the energy levels. We included in our final calculations all levels for $v=0$–65 in the $3\,^3\Pi$ state and for $v=0$–18 in the $4\,^3\Pi$ state. The calculations were used to fit measured levels up to $v=53$ in the $3\,^3\Pi$ state and up to $v=5$ in the $4\,^3\Pi$ state.

The theoretical calculations were fitted to experimental data for 288 rovibrational levels with predominantly $3\,^3\Pi$ character ($v=6$–53) and 22 rovibrational levels with predominantly $4\,^3\Pi$ character ($v=0$–5). The values of J for these data include 14, 16, 18, 20–29, 37, 39, 44, 46, 86, and

TABLE V. The parameters of the best fit for the off diagonal element of the diabatic Hamiltonian for the coupled $3\,^3\Pi$-$4\,^3\Pi$ system. The parameters are defined in Eq. (24); those marked with an asterisk (*) were not varied in the fit.

Parameter	Value	Parameter	Value
R_0^*	4.909 02 Å	A	366.86 cm^{-1}
γ^*	1.1744 Å^{-2}	B	160.72 cm^{-1}/Å

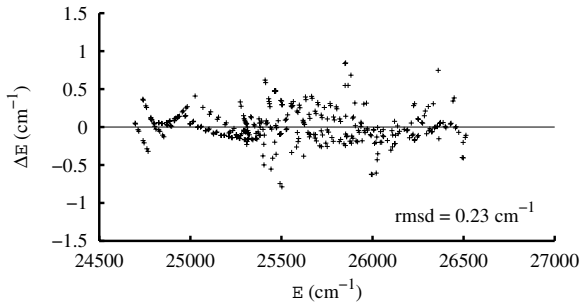

FIG. 7. The deviation of calculated rovibrational level energies of our fit from the experimental values. The 2×2 representation determined by our fit reproduces the $3\,^3\Pi$ and $4\,^3\Pi$ data with a rms deviation of 0.23 cm^{-1}.

88. Also included in the fit were 48 artificial levels for $v=0-5$ of the $3\,^3\Pi$ state ($J=14$, 16, 25, 27, 37, 39, 44, and 46). These levels were calculated using a single potential that fit the $v=6-12$ levels of the $3\,^3\Pi$ state. Without these levels as a constraint, the final fitted $3\,^3\Pi$ potential tended to have an unphysical, flat shape near its minimum. The parameters for the best fit are given in Tables IV and V, and a plot of the deviation between experiment and theory is shown in Fig. 7. The rms deviation of the best fit was 0.23 cm^{-1}, with all the original data included. The fit also gives us a measure of accuracy of the *ab initio* 2×2 diabatic potentials. The fitted diabatic potentials and the coupling term are shown in Fig. 8. The difference between the *ab initio* $3\,^3\Pi$ adiabatic potential inner and outer well depths is 480.0 cm^{-1}, whereas the difference between the well depths in the fitted $3\,^3\Pi$ adiabatic potential is 545.6 cm^{-1}. The *ab initio* equilibrium positions of the $3\,^3\Pi$ inner and outer wells are 4.13 and 6.12 Å, respectively, whereas the equilibrium positions in the fit are 3.98 and 5.71 Å.

EPAPS Table 2 (Ref. 44) tabulates the best-fit diabatic and adiabatic potentials. EPAPS Table 3 (Ref. 44) provides an extensive list of calculated energy levels and the comparison with experiment.

C. Effects of nonadiabatic coupling

An important conclusion of our calculations is that the nonadiabatic coupling between the $3\,^3\Pi$ and $4\,^3\Pi$ states is strong enough to couple levels that are not particularly close in energy. Although it would be appealing to be able to identify unperturbed levels of the $3\,^3\Pi$ and $4\,^3\Pi$ states that are not shifted except in the unusual case that a $3\,^3\Pi$ level is nearly degenerate with a $4\,^3\Pi$ level, this model is not justified for this system. Our results clearly indicate that the nonadiabatic coupling shifts all the levels investigated for the $4\,^3\Pi$ potential ($v=0-5$) as well as all levels of the $3\,^3\Pi$ potential in the same energy range.

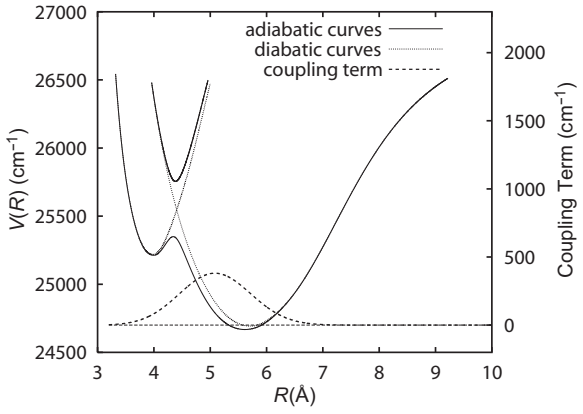

FIG. 8. The 2×2 diabatic representation that was fitted to the experimental data and the corresponding adiabatic potentials. The positions of the minimum energies for the inner and outer wells of the $3\,^3\Pi$ adiabatic potential are 3.98 and 5.71 Å, respectively. The difference in the energies calculated for the inner and outer minima of that potential is 545.6 cm^{-1}. (Compare Fig. 3, which gives the corresponding *ab initio* values.)

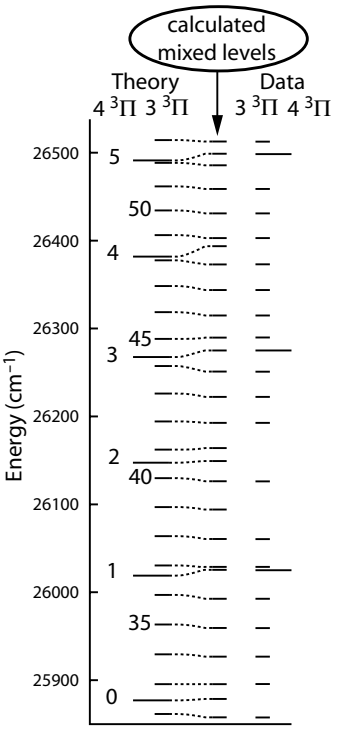

FIG. 9. Comparison of the fitted energy levels with experiment for $J=27$. Short horizontal lines correspond to levels with predominantly $3\,^3\Pi$ character while long horizontal lines correspond to levels with predominantly $4\,^3\Pi$ character. Vibrational numbers are indicated next to these lines.

Figure 9 illustrates this conclusion very clearly. The figure shows the comparison between experiment and theory for $J=27$. The right column shows the energy levels found experimentally. The left column shows the diagonal elements of the nonadiabatic Hamiltonian matrix [Eq. (12)], which correspond to "unperturbed energies" $E_{\alpha v}^{J(0)}$. The column marked "calculated mixed levels" gives the eigenvalues of the Hamiltonian matrix. The dotted lines show the effect of "turning on" the nonadiabatic coupling by multiplying the off diagonal elements of the full Hamiltonian by a factor ϵ that is varied from 0 to 1. One can see that every one of the energy levels is perturbed by the nonadiabatic coupling.

Unfortunately, unperturbed energies cannot be observed experimentally, so the calculated shifts cannot be measured. The experimental data show a regular spacing of $3\,^3\Pi$ levels interspersed with a few perturbed levels, suggesting that the $4\,^3\Pi$ state only adds local perturbations to the $3\,^3\Pi$ state. The local perturbations would correspond to $3\,^3\Pi$ energy levels shown in Fig. 9 that are nearly degenerate with a $4\,^3\Pi$ energy level. We have found that we can recover the interpretation of a local perturbation by considering second order perturbation theory (SOPT). The background shift of most of

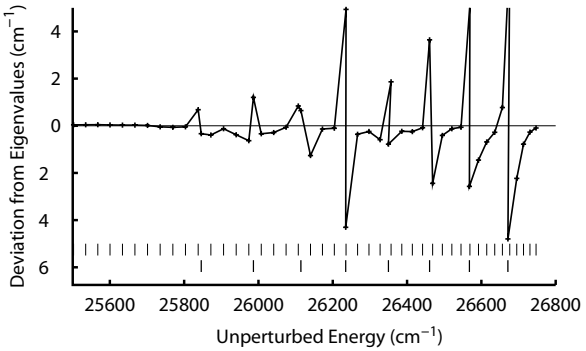

FIG. 10. Comparison of second order perturbation theory (SOPT) with matrix diagonalization. This figure shows the difference between SOPT, as modified using Eq. (25), and the exact eigenvalues calculated by matrix diagonalization. The abscissa is the unperturbed energy $E_{\alpha v}^{J(0)}$ of each state considered. The two rows of tic marks show the unperturbed energies of the 3 $^3\Pi$ (upper row) and the 4 $^3\Pi$ (lower row) states.

the levels in Fig. 9 is well described by SOPT. However, SOPT fails and even becomes singular when two unperturbed levels are degenerate. We found that a slight modification of SOPT can be used to "tame" the singularity,

$$\Delta E_{\alpha v}^{J} = \sum_{\alpha' v'} \frac{(H_{\alpha v,\alpha' v'}^{J})^2}{(E_{\alpha v}^{J(0)} - E_{\alpha' v'}^{J(0)}) + 4(H_{\alpha v,\alpha' v'}^{J})^2/(E_{\alpha v}^{J(0)} - E_{\alpha' v'}^{J(0)})}, \quad (25)$$

where $E_{\alpha v}^{J(0)}$ and $H_{\alpha v,\alpha' v'}^{J}$ are defined in Eqs. (10) and (12), respectively. The second term in the denominator, which we artificially added, is negligible for large values of $E_{\alpha v}^{J(0)} - E_{\alpha' v'}^{J(0)}$ but suppresses the singularity that normally occurs when $E_{\alpha v}^{J(0)} - E_{\alpha' v'}^{J(0)}$ is zero. This modification of SOPT accurately accounts for the overall background shift in the energy levels when the energy denominator $E_{\alpha v}^{J(0)} - E_{\alpha' v'}^{J(0)}$ is large and remains finite when the energy denominator is small. In Fig. 10 we have plotted the difference between the energy predicted by our modified SOPT and the result obtained by matrix diagonalization versus the unperturbed (diagonal) energies $E_{\alpha v}^{J(0)}$ of the nonadiabatic Hamiltonian matrix. This figure highlights the part of the shift that is not explained by SOPT, which is nearly zero for each level that is not very close to another level. However, when a 3 $^3\Pi$ and 4 $^3\Pi$ level are very close, there is a significant difference between the background shift predicted by SOPT and the exact shift. These are the levels where the perturbation is obvious in the experimental data.

If the 3 $^3\Pi$ levels that are shifted significantly more or less than the background shift—those that are close in energy to the 4 $^3\Pi$ levels—are neglected, the rest may be fitted to a potential curve in a fit that neglects the nonadiabatic coupling. This was done for the 3 $^3\Pi$ data by Morgus *et al.*[4] using the IPA method. This potential, while reproducing those states that were included with a rms deviation of 0.24 cm^{-1}, is an effective potential: it effectively includes the background shift that these levels feel. The present fit, which includes nonadiabatic coupling, has an overall shift in the range of the 4 $^3\Pi$ potential compared to the IPA potential. Furthermore, the fit reported here includes the energy levels that were excluded from the IPA fit. It reproduces this set of 3 $^3\Pi$ data with a rms deviation of 0.21 cm^{-1}.

It is not sensible to fit the energy levels of the 4 $^3\Pi$ state with an effective potential curve. Each 4 $^3\Pi$ level is relatively close in energy to one of the 3 $^3\Pi$ energy levels. The 4 $^3\Pi$ levels are perturbed in an irregular way, and one cannot pick out those that are more perturbed or less perturbed. The present fit, which includes nonadiabatic coupling, is able to reproduce the 4 $^3\Pi$ data with a rms deviation of 0.40 cm^{-1}.

The fitted energies also allowed us to identify 30 previously unassigned 3 $^3\Pi$ levels (up to v=56) and 12 previously unassigned 4 $^3\Pi$ levels (up to v=6). Comparisons of these measured and calculated level energies are also listed in EPAPS Table 3. Including these additional 42 levels, the rms deviation of the calculated energies from measured energies of all experimentally assigned 3 $^3\Pi$ ($6 \leqslant v \leqslant 56$) and 4 $^3\Pi$ ($0 \leqslant v \leqslant 6$) levels is only increased to 0.27 cm^{-1}.

V. CONCLUDING REMARKS

We have reported a comprehensive experimental and theoretical study of the coupled 3 $^3\Pi$ and 4 $^3\Pi$ states of NaK. Rovibrational energy levels and hyperfine structure were measured from near the minimum of the 3 $^3\Pi$ potential up to the region where levels belonging to both electronic states coexist and interact. The hyperfine signatures of the 3 $^3\Pi$ and 4 $^3\Pi$ states are very similar, but additional data from bound-free emission spectra were used to assign the electronic states. The mixing coefficients of strongly coupled levels could also be estimated from the data. The nonadiabatic coupling between the 3 $^3\Pi$ and 4 $^3\Pi$ states was formulated using a 2×2 diabatic representation of the electronic potentials. The diabatic electronic states and the coupling between them were simultaneously adjusted to fit the experimental data. This level of theory provides an excellent representation of all the measured rovibrational energy levels, including many perturbed levels that could not be fitted by a conventional single-channel analysis.

ACKNOWLEDGMENTS

This work was supported by the National Science Foundation Grant No. PHY-0244767. One of the authors (D.O.K.) was supported by the NSF REU site grant in the Department of Physics at Lehigh University; another author (L.M.) was supported by a NSF graduate fellowship. The authors acknowledge helpful conversations with Tom Bergeman and experimental assistance from Tyler Morgus.

APPENDIX: TWO- AND THREE-STATE MODEL

We consider the case in which two vibrational-electronic levels of the 3 $^3\Pi$ state interact with one of the 4 $^3\Pi$ state, forming a three-state system. For m=1, 2, and 3, the eigenstates $|m\rangle$ can be written as

$$|m\rangle = u_{m1}\chi_v^{(4)}|4\ ^3\Pi\rangle + u_{m2}\chi_{v'}^{(3)}|3\ ^3\Pi\rangle + u_{m3}\chi_{v''}^{(3)}|3\ ^3\Pi\rangle,$$

where the coefficients u_{mn} form a unitary matrix.

We assume that the observed total integrated intensity of the bound-free spectrum from state $|m\rangle$ can be expressed as

the sum of nonoverlapping contributions I_{m1} from the wavelength range of the $4\,^3\Pi$ component and I_{m2} from the wavelength range of the $3\,^3\Pi$ component,

$$I_{m1} = u_{m1}^2 \Gamma(4\,^3\Pi)\epsilon(4\,^3\Pi)\rho_m,$$

$$I_{m2} = (u_{m2}^2 + u_{m3}^2)\Gamma(3\,^3\Pi)\epsilon(3\,^3\Pi)\rho_m,$$

where $\Gamma(n\,^3\Pi)$ and $\epsilon(n\,^3\Pi)$ are the radiative rate and relative detection efficiency for $n\,^3\Pi \rightarrow 1(a)\,^3\Sigma^+$ transitions and ρ_m is the number density of the state $|m\rangle$.

The following ratios of the observed intensities eliminate the Γ's, ϵ's, and ρ's:

$$\alpha = \frac{I_{11}I_{32}}{I_{12}I_{31}} = \frac{u_{11}^2(u_{32}^2 + u_{33}^2)}{u_{31}^2(u_{12}^2 + u_{13}^2)},$$

$$\beta = \frac{I_{21}I_{32}}{I_{22}I_{31}} = \frac{u_{21}^2(u_{32}^2 + u_{33}^2)}{u_{31}^2(u_{22}^2 + u_{23}^2)}.$$

By straightforward analysis, we can transform the unitarity condition $\Sigma_{m=1}^3(u_{m2}^2+u_{m3}^2)=2$ into an equation for the unknown quantity $x=u_{32}^2+u_{33}^2$,

$$\frac{x}{\alpha(1-x)+x} + \frac{x}{\beta(1-x)+x} + x = 2.$$

The other mixing coefficients follow from x.

We can reduce these formulas to a two-state model for states $|1\rangle$ and $|3\rangle$ by uncoupling the state $|2\rangle$. In that case $u_{22}=1$, $\beta=0$, and we can identify $x=u_{33}^2=u_{11}^2=\cos^2\phi$ and $1-x=u_{13}^2=u_{31}^2=\sin^2\phi$, where

$$\cos^2\phi = \frac{\alpha^{1/2}}{1+\alpha^{1/2}}, \quad \sin^2\phi = \frac{1}{1+\alpha^{1/2}}.$$

[1] J. Huennekens, I. Prodan, A. Marks, L. Sibbach, E. Galle, T. Morgus, and Li Li, J. Chem. Phys. **113**, 7384 (2000).
[2] P. Burns, L. Sibbach-Morgus, A. D. Wilkins, F. Halpern, L. Clarke, R. D. Miles, Li Li, A. P. Hickman, and J. Huennekens, J. Chem. Phys. **119**, 4743 (2003).
[3] P. Burns, A. D. Wilkins, A. P. Hickman, and J. Huennekens, J. Chem. Phys. **122**, 074306 (2005).
[4] L. Morgus, P. Burns, R. D. Miles, A. D. Wilkins, U. Ogba, A. P. Hickman, and J. Huennekens, J. Chem. Phys. **122**, 144313 (2005).
[5] A. D. Wilkins, L. Morgus, J. Hernandez-Guzman, J. Huennekens, and A. P. Hickman, J. Chem. Phys. **123**, 124306 (2005).
[6] Li Li and R. W. Field, J. Phys. Chem. **87**, 3020 (1983).
[7] X. Xie and R. W. Field, J. Mol. Spectrosc. **117**, 228 (1986).
[8] Li Li and R. W. Field, J. Mol. Spectrosc. **123**, 237 (1987).
[9] Li Li, Q. Zhu, and R. W. Field, J. Mol. Spectrosc. **134**, 50 (1989).
[10] Li Li, Q. Zhu, and R. W. Field, Mol. Phys. **66**, 685 (1989).
[11] Li Li, A. M. Lyrra, W. T. Luh, and W. C. Stwalley, J. Chem. Phys. **93**, 8452 (1990).
[12] T.-J. Whang, A. M. Lyyra, W. C. Stwalley, and Li Li, J. Mol. Spectrosc. **149**, 505 (1991).
[13] T.-J. Whang, W. C. Stwalley, Li Li, and A. M. Lyyra, J. Mol. Spectrosc. **155**, 184 (1992).
[14] Li Li, T. An, T.-J. Whang, A. M. Lyyra, W. C. Stwalley, R. W. Field, and R. A. Bernheim, J. Chem. Phys. **96**, 3342 (1992).
[15] D. S. Chen, L. Li, X. T. Wang, Li Li, Q. Hui, H. Ma, L. Q. Li, X. Y. Xu, and D. Y. Chun, J. Mol. Spectrosc. **161**, 7 (1993).
[16] A. Yiannopoulou, B. Ji, Li Li, M. Li, K. Urbanski, A. M. Lyyra, W. C. Stwalley, and G.-H. Jeung, J. Chem. Phys. **101**, 3581 (1994).
[17] B. Ji, C.-C. Tsai, Li Li, T.-J. Whang, A. M. Lyyra, H. Wang, J. T. Bahns, W. C. Stwalley, and R. J. Le Roy, J. Chem. Phys. **103**, 7240 (1995).
[18] Y. Liu, J. Li, M. Xue, D. Chen, Li Li, and G.-H. Jeung, J. Chem. Phys. **103**, 7213 (1995).
[19] J. T. Kim, H. Wang, C.-C. Tsai, J. T. Bahns, W. C. Stwalley, G. Jong, and A. M. Lyyra, J. Chem. Phys. **102**, 6646 (1995); **103**, 9891(E) (1995).
[20] Li Li, A. Yiannopoulou, K. Urbanski, A. M. Lyyra, B. Ji, W. C. Stwalley, and T. An, J. Chem. Phys. **105**, 6192 (1996); **106**, 8626(E) (1997).
[21] J. Li, Y. Liu, H. Gao, M. Xue, D. Chen, and Li Li, J. Mol. Spectrosc. **175**, 13 (1996).
[22] Y. Liu, J. Li, H. Gao, D. Chen, Li Li, R. W. Field, and A. M. Lyyra, J. Chem. Phys. **108**, 2269 (1998).
[23] J. Li, Y. Liu, H. Chen, H. Gao, J. Xiang, D. Chen, G. Wu, Li Li, and R. W. Field, J. Chem. Phys. **108**, 7707 (1998).
[24] V. S. Ivanov, V. B. Sovkov, Li Li, A. M. Lyyra, G. Lazarov, and J. Huennekens, J. Mol. Spectrosc. **194**, 147 (1999).
[25] C. Linton, F. Martin, A. J. Ross, I. Russier, P. Crozet, A. Yiannopoulou, Li Li, and A. M. Lyyra, J. Mol. Spectrosc. **196**, 20 (1999).
[26] Li Li and A. M. Lyyra, Spectrochim. Acta, Part A **55**, 2147 (1999).
[27] G. Lazarov, A. M. Lyyra, Li Li, and J. Huennekens, J. Mol. Spectrosc. **196**, 259 (1999).
[28] X. Dai, J. O. Clevenger, Y. Liu, M. Song, J. Shang, D. Chen, R. W. Field, and Li Li, J. Mol. Spectrosc. **200**, 120 (2000).
[29] Li Li, X. Dai, Y. Liu, J. O. Clevenger, R. W. Field, G.-H. Jeung, N. Geum, and A. M. Lyrra, J. Mol. Spectrosc. **205**, 139 (2001).
[30] M. Oppenheimer, J. Chem. Phys. **57**, 3899 (1972).
[31] H. Lefebvre-Brion and R. W. Field, *The Spectra and Dynamics of Diatomic Molecules* (Elsevier, San Diego, CA, 2004).
[32] S. Magnier and Ph. Millié, Phys. Rev. A **54**, 204 (1996).
[33] S. Magnier, M. Aubert-Frécon, and Ph. Millié, J. Mol. Spectrosc. **200**, 96 (2000).
[34] T. Pacher, L. S. Cederbaum, and H. Köppel, J. Chem. Phys. **89**, 7367 (1988).
[35] J. A. Spirko, J. T. Mallis, and A. P. Hickman, J. Phys. B **33**, 2395 (2000).
[36] A. P. Hickman, R. D. Miles, C. Hayden, and D. Talbi, Astron. Astrophys. **438**, 31 (2005).
[37] S. Gerstenkorn and P. Luc, *Atlas du Spectre D'Absorption de la Molécule D'Iode* (CNRS, Paris, 1978).
[38] L. Morgus, Ph.D. thesis, Lehigh University, 2005.
[39] R. J. Le Roy, University of Waterloo, Chemical Physics Research Report No. CP-661 (2005); http://leroy.uwaterloo.ca/programs/
[40] M. W. Schmidt, K. K. Baldridge, J. A. Boatz *et al.*, J. Comput. Chem. **14**, 1347 (1993).
[41] T. H. Dunning, Jr. and P. J. Hay, in *Methods of Electronic Structure Theory*, edited by H. F. Shaeffer III (Plenum, New York, 1977), Chap. 1, pp. 1–27.
[42] A. Szabo and N. S. Ostlund, *Modern Quantum Chemistry: Introduction to Advanced Electronic Structure Theory* (Macmillan, New York, 1982).
[43] B. C. Carlson and J. M. Keller, Phys. Rev. **105**, 102 (1957).
[44] See EPAPS Document No. E-JCPSA6-125-004636 for three tables of related information. This document can be reached via a direct link in the online article's HTML reference section or via the EPAPS homepage (http://www.aip.org/pubservs/epaps.html).
[45] See EPAPS Document No. E-JCPSA6-122-023515 for five tables of related information. This document can be reached via a direct link in the online article's HTML reference section or via the EPAPS homepage (http://www.aip.org/pubservs/epaps.html).
[46] A. Pashov, W. Jastrzębski, and P. Kowalczyk, Comput. Phys. Commun. **128**, 622 (2000).
[47] B. S. Garbow, K. E. Hillstrom, and J. J. Moore, subroutines LMDIF and LMDIF1 from the MINPACK library, available from http://www.netlib.org